Supplement of Atmos. Chem. Phys., 24, 5247–5263, 2024
https://doi.org/10.5194/acp-24-5247-2024-supplement

Atmospheric Chemistry and Physics
Open Access
EGU

Supplement of

Secondary ice production – no evidence of efficient rime-splintering mechanism

Johanna S. Seidel et al.

Correspondence to: Susan Hartmann (susan.hartmann@tropos.de)

S1 Ice crystal detection limit

S1.1 Characterization of the Ice Counter

The IC is based on the principle of a conventional impactor (Kulkarni, 2011). To determine the impaction efficiency of particles in the specifically designed IC, the theoretical particle aerodynamic cut-off diameter $D_{\mathrm{p},50}$ was derived by applying the circular jet model (e.g., Hinds, 1999) and verified by additional characterization experiments. Particles larger than the $D_{\mathrm{p},50}$ tend to impact on the substrate as their inertia causes them to escape the airflow, while particles smaller than the $D_{\mathrm{p},50}$ tend to follow the streamlines of the air flow. In general, $D_{\mathrm{p},50}$ is defined as particle diameter at which particles impact with a probability of 50% and can be described as:

$$D_{\mathrm{p},50} = \sqrt{\frac{9\,\eta\,W\,Stk_{50}}{\rho_{\mathrm{p}}\,C_{\mathrm{c}}\,U}}, \tag{1}$$

with air viscosity η, nozzle diameter W, particle density ρ_{p} and Stokes number $Stk_{50} = 0.24$ (circular jet) corresponding to $D_{\mathrm{p},50}$ for $500 \leq Re \leq 3000$, slip correction C_{c} and jet velocity $U = \frac{Q}{\pi\left(\frac{W}{2}\right)^2}$, and volumetric flow rate Q. C_{c} can be calculated by $C_{\mathrm{c}} = 1 + \frac{\lambda_{\mathrm{g}}}{d_{\mathrm{p}}}\left(2.34 + 1.05\exp\left(-0.39\frac{D_{\mathrm{p}}}{\lambda_{\mathrm{g}}}\right)\right)$, with λ_{g} the mean free path of air and particle diameter D_{p}. $D_{\mathrm{p},50}$ depends on the nozzle diameter W with smaller nozzle diameters leading to smaller $D_{\mathrm{p},50}$. The IC has been constructed with the possibility to exchange different nozzle diameters (W = 3.0 mm, 3.5 mm, 4.0 mm). The theoretical description of $D_{\mathrm{p},50}$ is valid for particles impacting on a solid plate. For the IDEFIX IC, a viscous aqueous solution is used as the impaction surface. The air flow is directed perpendicular to the sugar solution and deforms the surface, which further complicates the theoretical description of particle impaction. To overcome this difficulty, experiments with air-suspended monodisperse polystyrene latex particles (PSL ranging from 1 μm to 4.5 μm) were conducted to measure the impaction efficiency for this setup for different air flow rates and nozzle diameters. PSL particles are guided either through the IC or through a bypass and the corresponding particle number concentration were measured with WELAS®. Then, the impaction efficiency of the IC is determined by dividing particle number concentration measured downstream the IC with particle number concentration of the bypass air flow. The results are summarized in Table S1. Verification experiments showed that the essential behavior is represented by the theoretical model. In detail, experimentally determined $D_{\mathrm{p},50}$ values are smaller than the theoretical description, resulting in a better collection efficiency for this specific setup of the IC.

S1.2 Sublimation of secondary ice particles in IDEFIX

The impaction characteristics of particles in the IC and sublimational effects limit the detectable size of SI particles. At the current configuration of IDEFIX, SI particles with 3.3 μm in diameter would shrink to 2 μm on their pathway into the IC considering the worst case scenario of saturation conditions with respect to ice (Fig. S1). With this, such particles will be impacted in the IC with an efficiency of 50 %. If SI particles have smaller diameters than 3.3 μm at their production, the probability that they will be counted within the IC decreases significantly. Therefor, this size is assumed to be the lower detection limit.

Table S1. Impaction efficiency of different sized PSL particles was experimentally determined for different ice counter impactor nozzle diameters and volume flows. The corresponding theoretical particle cut-off diameter with 50% impaction efficiency based on the circular jet impaction model from Hinds (1999) are given.

nozzle diameter [mm]	volume flow [$\mathrm{L\,min^{-1}}$]	circular jet model $D_{p,50}$ [μm]	measured impaction efficiency of D_{PSL} 1.0 μm	2.0 μm	3.0 μm	4.5 μm
3.0	5.25	3.00	0	0.06	**0.54**	1.00
	6.75	2.76		0.16	0.62	
	8.24	2.50	0.08	0.25	0.66	
3.5	5.25	3.95		0.00	0.22	1.00
	6.75	3.48		0.00	**0.52**	1.00
	8.24	3.15		0.34	**0.55**	1.00
	12.35	2.57		**0.5; 0.57**		
4.0	6.75	4.21			0.27	
	8.24	3.82			0.38	
	12.35	3.10	0.13	0.39	0.76	1.00

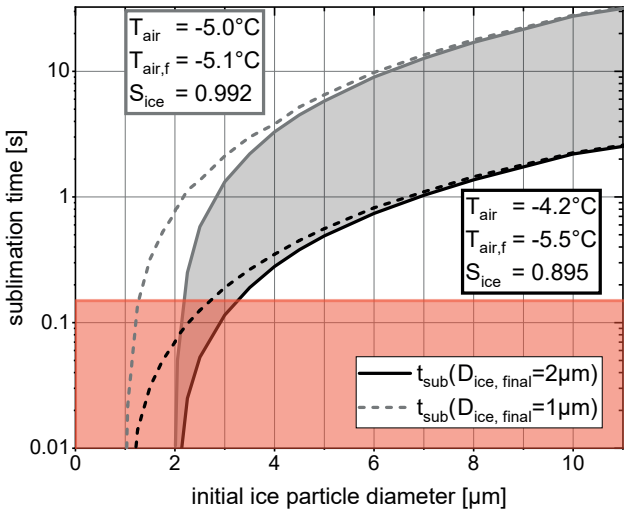

Figure S1. Sublimation time as a function of initial ice particle diameter. Ice particles are assumed to have a spherical shape and experience different levels of subsaturation with respect to ice. The time it takes to sublimate to a final ice particle size of $D_{\mathrm{ice,final}} = 2\,\mu\mathrm{m}$ (solid lines, light gray shaded area) and 1 μm (dashed lines) are shown since they correspond to expected IC counting efficiencies of 50 % and significant below 50 %, respectively. Two extreme scenarios span the relevant parameter space regarding temperature T, frost point $\mathrm{T_f}$ and respective saturation with respect to to ice $\mathrm{S_{ice}}$ representative for an IDEFIX experiment, i.e., almost ice saturation (gray line) at set temperature and 90 % saturation accounting for temperature and humidity uncertainties (black line). The residence time from ice target to supercooled sugar solution surface is given (red line). When sublimation time is shorter than residence time (red area), ice particles are detected with less than 50 % for $D_{\mathrm{ice,final}} = 2\,\mu\mathrm{m}$ and might be to small to be detected for $D_{\mathrm{ice,final}} = 1\,\mu\mathrm{m}$.

S2 Determination of the collision rates during riming

S2.1 Methods

Droplet-graupel collision rates influence rimer microphysical processes and are relevant statistical parameters to describe SIP rates. Hence, they are crucial parameters for the comparability to other rime-splintering experiments. The collision rates can be expressed in terms of mass and number of accreted supercooled droplets, respectively. For reasons of comparability, the collision rates are normalized to the graupel's geometrical cross sectional area perpendicular to the flow direction ($\mathrm{A_{cross}}$). An average mass collision rate, also called mass accretion rate ($\mathrm{R_{accr,M}}$) in the following, can be calculated from the frozen droplet mass accreted on the initial ice target (ΔM_{accr}) in a certain time interval (Δt):

$$R_{\mathrm{accr,M}} = \frac{1}{\mathrm{A_{cross}}} \frac{\Delta M_{\mathrm{accr}}}{\Delta t}. \tag{2}$$

To derive the number accretion rate, the mass accretion rate (Eq. 2) is divided by the mean mass of the number size distribution of the accreted droplets $< M_d >= \frac{\pi}{6}\rho_{\mathrm{w}}\frac{M_3}{M_0}$, with M_0 and M_3 being the $0th$ and $3rd$ moment of the distribution $n_{\mathrm{accr}}(D)$. From additional WELAS® measurements, the airborne droplet number size distribution $n(D)$ is found to be log-normal distributed. Since the normalized size distribution of airborne droplets $n^*(D) = \frac{n(D)}{M_0} = \frac{n(D)}{\int n(D')\mathrm{d}logD'}$ is not influenced by riming, i.e. the shape of the normalized DSD does not change comparing measurements without and with an ice target (Fig. S2), we assume $n^*(D)$ to represent the normalized accreted DSD and the following is obtained

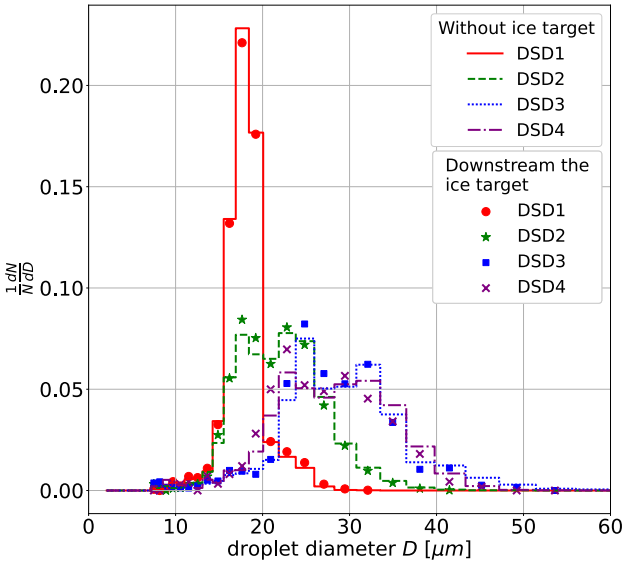

Figure S2. Measurements of the droplet size distributions DSD1-4 without (lines) and downstream (symbols) an ice target at -5 °C and $1\,\mathrm{m\,s^{-1}}$.

$$R_{\mathrm{accr,N}} = \frac{R_{\mathrm{accr,M}}}{< M_d >} = \frac{6}{\pi\rho_{\mathrm{w}}} \frac{1}{\int D'^3 n^*(D')\mathrm{d}logD'} R_{\mathrm{accr,M}}. \tag{3}$$

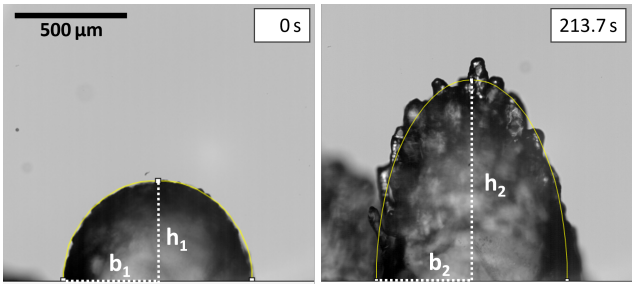

Figure S3. HSV-images showing a nearly spherical ice target before (left) and more ellipsoidal shaped ice target during riming (right). In this example droplets of DSD2 are accreted on the fixed ice target with an air flow velocity of $1\,\mathrm{m\,s^{-1}}$ at $-5\,°\mathrm{C}$. The adjusted semi-ellipse of the rimer top is depicted in yellow together with the two half-axes of the semi ellipse: height h and width b.

Currently, the IDEFIX setup does not allow a direct measurement of the ice target weight before and after riming. To determine the mass accretion rate for a representative set of experiments, the increase of rimer mass in a certain time interval Eq. (2) was derived via two different and mostly independent methods using a) 2D information from HSV images, and b) the rimer surface temperature from IR thermography as input parameter for a heat balance model of graupel adopted from Pruppacher and Klett (2010).

Considering the first method, the accreted mass per time period was estimated from the projected rimer surface area as seen on the HSV images (Fig. S3). Since the ice target is attached to a cross of carbon fibers and therefor has no rotational degree of freedom, the riming occurs only on the upper part of the ice target. Neglecting microscopic rimer surface structure, the projected area of the rimer in matured stage was observed to take on a semi-ellipsoidal shape. Using the freely accessible image analysis tool imageJ, the respective half width b_2 and height h_2 are determined (Fig. S3, right). In doing so, the half ellipse was adjusted to be fully within the visible graupel area of the HSV image. The volume increase due to accretion of droplets observed between two different time steps is calculated assuming rotational symmetry and subtracting the determined ice target volumes. Following this approach, the uncertainty results either from air cavities within the rimer body or rime spire structures that are grown beyond the ellipsoid and is assumed to be approx. 10% in volume. To obtain the accreted rimer mass from the derived volume increase, a rimer density was assumed.

Via the second method, the mass accretion rates were calculated by applying the heat balance model of a riming particle given in Pruppacher and Klett (2010) using the rimer surface temperature from infrared thermography as input data. Assuming steady state conditions and a constant surface temperature, the heat q and mass m transfer at a riming ice particle becomes simplified to Eq. (4) (Pruppacher and Klett, 2010, p. 680-681).

$$\left(\frac{dq}{dt}\right)_{\mathrm{diff,h}} + \left(\frac{dq}{dt}\right)_{\mathrm{diff,m}} + \left(\frac{dq}{dt}\right)_{\mathrm{accr}} + \left(\frac{dq}{dt}\right)_{\mathrm{fr}} = 0 \tag{4}$$

The contributing terms to the riming heat balance, illustrated in Fig. S4, are (i) the heat dissipation to the environment:

$$\left(\frac{dq}{dt}\right)_{\mathrm{diff,h}} = -\frac{A_{\mathrm{tar}} k_{\mathrm{a}} Nu (T_{\mathrm{tar,s}} - T_{\mathrm{env}})}{D_{\mathrm{tar}}} \tag{5}$$

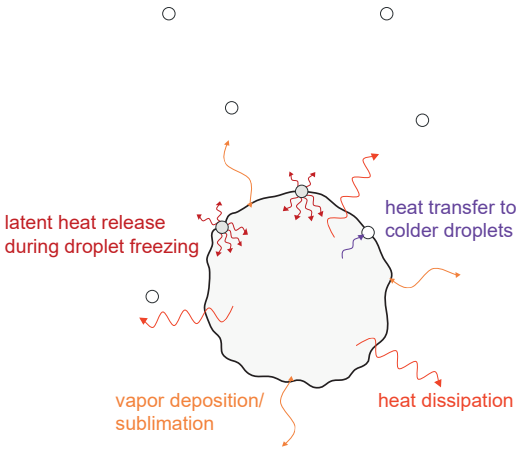

Figure S4. Schematics of the relevant heat transfer of a riming ice particle.

with target surface area A_{tar} and target diameter D_{tar}, thermal conductivity of dry air k_{a} (param. in Beard and Pruppacher, 1971), Nusselt number $Nu = 0.88 Re^{\frac{1}{2}} Pr^{\frac{1}{3}}$ including Reynolds Re and Prandtl Pr number, temperature of the ice target surface $T_{\mathrm{tar,s}}$ and of the humid air environment T_{env}; (ii) heating rate due to vapor deposition or sublimation:

$$\left(\frac{dq}{dt}\right)_{\mathrm{diff,m}} = L_{\mathrm{s}} \left(\frac{dm}{dt}\right)_{\mathrm{diff}} \tag{6}$$

with latent heat of sublimation L_{s} (param. in Murphy and Koop, 2005) and diffusional growth term, which can be written as

$$\left(\frac{dm}{dt}\right)_{\mathrm{diff}} = \frac{A_{\mathrm{tar}} D_{\mathrm{v}} M_{\mathrm{w}} Nu}{D_{\mathrm{tar}} R^*} \left(\frac{e_{\mathrm{env}}}{T_{\mathrm{env}}} - \frac{e_{\mathrm{tar,s}}}{T_{\mathrm{tar,s}}}\right) \tag{7}$$

including diffusivity of water vapor in air D_{v} (param. in Hall and Pruppacher, 1976), molar weight of water $M_{\mathrm{w}} = 0.01801\,\mathrm{J\,kg^{-1}}$, ideal gas constant $R^* = 8.31446\,\mathrm{J\,mol^{-1}\,K^{-1}}$, temperature and water vapor partial pressure over ice of the environment (T_{env}, e_{env}) and target surface ($T_{\mathrm{tar,s}}$, $e_{\mathrm{tar,s}}$), respectively; (iii) heating rate to warm accreted droplets:

$$\left(\frac{dq}{dt}\right)_{\mathrm{accr,h}} = -c_{\mathrm{w}} (T_{\mathrm{tar}} - T_{\mathrm{env}}) \left(\frac{dm}{dt}\right)_{\mathrm{accr}} \tag{8}$$

with heat capacity of supercooled water c_{w} (Biddle et al., 2013) and mass accretion rate $\left(\frac{dm}{dt}\right)_{\mathrm{accr}}$ and finally, (iv) latent heat release due to freezing of accreted droplets

$$\left(\frac{dq}{dt}\right)_{\mathrm{fr}} = L_{\mathrm{f}} \left(\frac{dm}{dt}\right)_{\mathrm{accr}} \tag{9}$$

with the latent heat of fusion L_f (Pruppacher and Klett, 2010, p.97) and the mass accretion rate $\left(\frac{dm}{dt}\right)_\mathrm{accr}$ to be determined, which describes the mass increase per time interval due to accretion of colliding and subsequent freezing supercooled droplets during riming. Solving the rimer heat balance equation (Eq. 4) for the mass growth rate due to droplet accretion $\left(\frac{dm}{dt}\right)_\mathrm{accr}$ results in the following expression:

$$\left(\frac{dm}{dt}\right)_\mathrm{accr} = \frac{-\left(\frac{dq}{dt}\right)_\mathrm{diff,h} - \left(\frac{dq}{dt}\right)_\mathrm{diff,m}}{L_\mathrm{f} - c_\mathrm{w}(T_\mathrm{tar,s} - T_\mathrm{env})} \tag{10}$$

To describe the rimer surface area, the graupel was assumed to compose of a half sphere at the bottom and a rotation-symmetric semi-ellipsoid on top. The graupel diameter and the height of the semi-ellipsoid were determined in analogy to the first method. Applying the heat-balance model to calculate the mass accretion rate, it must be distinguished between dry and wet growth conditions. Eq. 10 is valid for riming in the dry growth regime. During wet growth, the surface temperature increases to the melting point enabling liquid layer formation on the rimer top and thus, $\left(\frac{dq}{dt}\right)_\mathrm{diff,m}$ is a function of latent heat of evaporation instead of sublimation and the water vapor partial pressure at the target surface is considered over water instead of over ice. To get an idea of the scales of the terms contributing to the heat balance equation (Eq. 4), which is the basis for Eq. 10, the individual terms were calculated for the examples of dry, wet, and transition growth presented in Fig. 4, Sect. 3.1 and are given in Table S2.

Table S2. Heat balance of a riming ice particle for three examples of dry, wet and transitional growth (Fig. 4a,b,c). The surface temperature elevation is applied as input parameter to calculate the contributions of the different heat fluxes.

growth regime	dT [K]	$\left(\frac{dq}{dt}\right)_\mathrm{fr}$ [mW]	$\left(\frac{dq}{dt}\right)_\mathrm{diff,h}$ [mW]	$\left(\frac{dq}{dt}\right)_\mathrm{diff,m}$ [mW]	$\left(\frac{dq}{dt}\right)_\mathrm{accr}$ [mW]
dry (C2_T39)	0.6	0.33	−0.21	−0.11	−0.00
wet (C2_T56)	4.94	3.34	−1.87	−1.32	−0.21
transition (C2_T50)					
dry limit	5.03	7.32	-4.62	-2.50	-0.50
wet limit	8.03	12.16	-7.37	-4.11	-1.32

S2.2 Number and mass collision rates

Both independent methods described in Supplement Sect. S2.1 were used to derive the collision rates in dependence of the DSD for a subset of experiments at different thermodynamic conditions. The compilation of number and mass collision rates determined from methods (a) and (b) is presented in Fig. S5.

Using 2D information from HSV images (method a), the following input parameter are applied. In addition to diameter and height of the rimed ice target, the graupel density is needed to calculate the accreted rimer mass (Eq. 2,3). In general, the graupel density can vary greatly depending on formation conditions. Due to the fact, that the graupel density and thus the volume of air cavities within the graupel structure can not be determined at the IDEFIX experiments, a density of $0.9\,\mathrm{g\,m^{-3}}$, corresponding to compact ice without any air spaces, is assumed as an upper limit. Parameterizations of graupel density from Cober and List (1993) and Heymsfield and Pflaum (1985), where it is a function of the rimer surface temperature, the impact velocity and the median radius of the accreted cloud droplets (Macklin, 1962), are applied as lower limit. The mean values and the

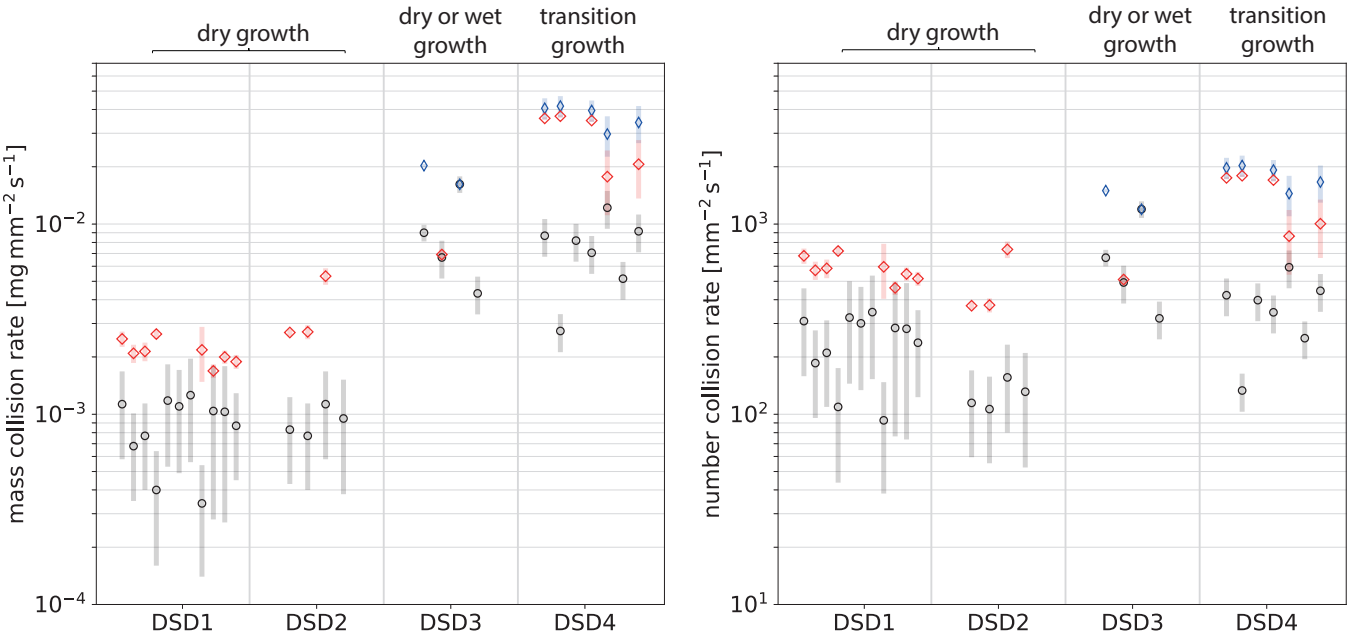

Figure S5. Mass and number collision rates grouped by droplet size distributions DSD1–4 and correspondingly observed growth regime. Average collision rates derived each via method (a) (black open circles) and method (b) based on the heat balance model assuming either a frozen ice target surface (dry growth conditions, red open diamonds) or a liquid water surface (wet growth conditions, blue open diamonds) depending on case. For the transition regime resulting from DSD4, the HSV-image based collision rates represent an average value accounting for the relevant ice density range (gray shaded bars), while applying the heat-balance method an upper (considering wet growth) and lower (considering dry growth) range is given.

possible range according to variable rimer densities are represented as symbols and gray shaded bars in Fig. S5, respectively. The number collision rates are obtained by accounting for the respective DSDs.

Applying method (b) – the determination of mass and number accretion rate derived from the heat balance model according to Pruppacher and Klett (2010) – steady state conditions can be assumed as the rimer surface temperature increases to a constant value in first approximation (see Sect. 3.1). Therefore, Eq. (10) is easy to solve and inserted into Eq. (2). The surface temperature elevation during riming derived from infrared thermography, target diameter and rimer surface area determined from HSV images are applied as input parameter. Thereby, it is discriminated between the dry and wet graupel growth regime by accounting for the respective properties of the ice or liquid water surface in Eq. (10). For transitional growth (alternating ice and liquid water surface) both growth regimes are applied. Due to an inhomogeneous distribution of the surface temperature, the collision rates are calculated by using the average surface temperature displayed as symbol in Fig. S5 and the range of surface temperature variation is represented as bars.

Droplet–rimer collisions of DSD1 and DSD2 result in average number and mass collision rates of $3.6 \times 10^{2}\,\mathrm{mm^{-2}\,s^{-1}}$ and $1.6 \times 10^{-3}\,\mathrm{mg\,mm^{-2}\,s^{-1}}$, respectively. For DSD3 and DSD4 the respective average number and mass collision rates are higher with $8.7 \times 10^{2}\,\mathrm{mm^{-2}\,s^{-1}}$ and $1.6 \times 10^{-2}\,\mathrm{mg\,mm^{-2}\,s^{-1}}$, respectively, enabling the transition to wet growth. Comparing the approaches, method (b) results almost always in a factor of 2 to 4 times higher accretion rates than method (a) independently of the applied droplet size distribution. A possible reason for the discrepancy between the results of both methods is probably

the simplified assumption of the ice target surface. However, it is remarkable that two independent approaches achieve nearly similar collision rates.

To assess the atmospheric relevant parameter space of number and mass accretions rates during riming for different cloud convection types, there are almost no atmospheric observations available. From ground-based observations and theoretical considerations, Erfani and Mitchell (2017) derived mass collision rates on the order $10^{-5}\,\mathrm{mg\,mm^{-2}\,s^{-1}}$ for frontal clouds considering liquid water contents (LWCs) from $0.05\,\mathrm{g\,m^{-3}}$ to $0.2\,\mathrm{g\,m^{-3}}$ and cloud droplets of median mass diameter 8 μm and 16 μm. Jensen and Harrington (2015) simulated similar mass collision rates of 2–$5 \times 10^{-5}\,\mathrm{mg\,mm^{-2}\,s^{-1}}$ for LWC of 0.3 g $\mathrm{m^{-3}}$ and droplet mean diameter between 10 μm and 24 μm. Since the estimated LWC and the mass accretion rates in the IDEFIX experiments are at least two orders of magnitude above this, it can be assumed that the riming conditions at IDEFIX are more representative for convective clouds.

S3 Melting point calibration of IR camera

In the experiments in which wet graupel growth could be observed with the HSV camera due to the visible formation of liquid layers on top of the rimer surface, the IR-measured maximum of the surface temperature during riming was not reaching 0 °C, but appearing between -1 °C and -2 °C. To check, whether the measured temperature maximum corresponds to the physical melting point of water, a calibration was done. Therefore, a spherical target made from epoxy resin adhesive was inserted into the IDEFIX chamber and a cap of liquid water with roughly diameter of 0.5–1 mm was generated on the top of it. Ice crystals were then inserted into the chamber by putting the tip of a screwdriver covered with ice (it was shortly dipped into liquid nitrogen) through one of the corona needle slots into the head section of IDEFIX. Once the liquid cap was hit by an ice crystal, the freezing was initiated and the rapid spread of dendritic ice structures over the liquid could be captured with the HSV camera. From parallel surface temperature monitoring of the IR camera, we obtained a surface temperature maximum of -1.4 ± 0.6 K (average of three experiments, uncertainty range of 3σ) in the moment of freezing, where the liquid cap physically should have a temperature of 0 °C.

S4 Freezing and inter-arrival time of accreted droplets on ice surface

To calculate the individual freezing time and the inter-arrival time of two consecutive droplets hitting the same site, we consider the following system (Fig. S6): a supercooled droplet with a diameter of D_d and a volume of V_d in an air stream is assumed to have the same temperature as the environment $T_\mathrm{d} = T_\mathrm{env}$. After collision with the large rimer surface, the supercooled water droplet forms a spherical liquid cap with contact angle θ at the water-air-ice interface (observation described in Sect. 3.1) and radius $a = r \sin\theta$ whereby r is the radius of the imaginary sphere. During freezing, the temperature of the spherical cap rises to the melting point of water $T_\mathrm{d} = T_0 = 273.15\,\mathrm{K}$. The freezing time of the droplets can be approximated with the time of the second freezing stage, since the initial freezing and the adaptation to the ambient temperature after freezing happen on a much smaller time scale and are therefore negligible (Pruppacher and Klett, 2010; Korolev and Leisner, 2020).

The freezing time t_2 is determined by the transfer of latent heat to the surrounding air $q_\mathrm{cap-air}$ and the ice body $q_\mathrm{cap-ice}$. Solving the heat balance equation for a ventilated spherical droplet cap on an ice substrate according to Macklin and Payne

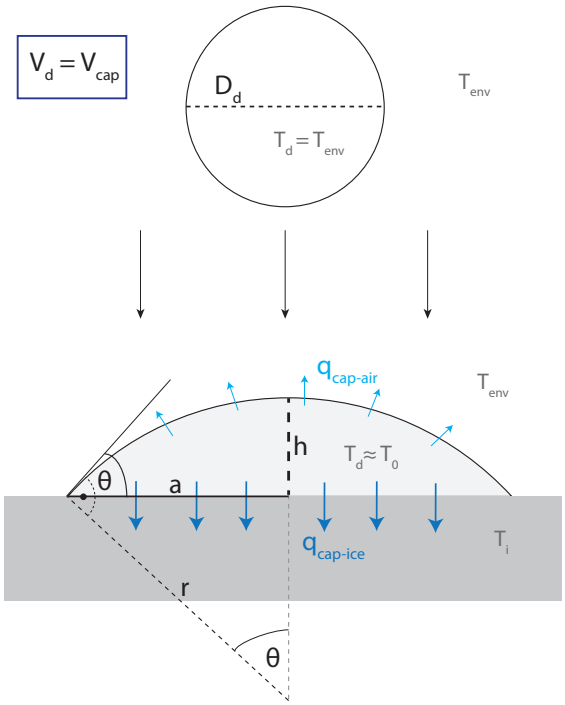

Figure S6. Geometry of a supercooled droplet ($T_\mathrm{d} < T_0 = 273.15\,\mathrm{K}$) of diameter D resulting in a freezing spherical cap with contact angle θ, base radius a, height h and radius of the imaginary sphere r on an ice surface of temperature T_i after collision. Heat released during the freezing process of the droplet water is transferred to the environmental air ($q_{\mathrm{cap-air}}$) of temperature T_env and to the ice surface ($q_{\mathrm{cap-ice}}$).

(1968) (cited in Pruppacher and Klett, 2010) and allowing for a variable contact angle yields

$$\alpha t_2 + \beta\sqrt{t_2} - \gamma = 0 \tag{11}$$

with

$$\alpha = 2\pi \frac{D_\mathrm{d}\sin\theta}{(2(2+\cos\theta)(1-\cos\theta)^2)^{\frac{1}{3}}} \bar{f}[k_a(T_0 - T_\mathrm{env}) + L_e D_v(\rho_{\mathrm{v,a}} - \rho_{\mathrm{v,env}})],$$

$$\beta = (T_0 - T_\mathrm{cap}) k_\mathrm{i} \frac{D_\mathrm{d}^2(\sin\theta)^2}{(2(2+\cos\theta)(1-\cos\theta)^2)^{\frac{2}{3}}} \sqrt{\frac{\rho_\mathrm{i} c_\mathrm{i} \pi}{k_\mathrm{i}}},$$

$$\gamma = -\frac{\pi}{6} D_\mathrm{d}^3 \rho_\mathrm{w}[L_\mathrm{f} - c_\mathrm{w}(T_0 - T_{env})],$$

The analytical solution for t_2 is

$$t_2 = \left(\frac{-\beta + \sqrt{\beta^2 - 4\alpha\gamma}}{2\alpha}\right)^2. \tag{12}$$

Thereby $q_{\mathrm{cap-air}} = \alpha t_2$ and $q_{\mathrm{cap-ice}} = \beta\sqrt{t_2}$. γ is the total amount of released heat. $\bar{f}$ is the mean ventilation coefficient ($\bar{f} = 1.5$), k_{a} represents the thermal conductivity of dry air (param. in Beard and Pruppacher, 1971; Pruppacher and Klett, 2010, p. 508). k_{i} is the thermal conductivity of ice (param. in Pruppacher and Klett, 2010, p. 676). L_{e} and L_{f} are the latent heats of evaporation and freezing (param. in Pruppacher and Klett, 2010, p. 97), respectively. Further, the diffusivity of water in air D_{v} (param. in Pruppacher and Klett, 2010, p. 503), the water vapor densities of air at the cap surface $\rho_{\mathrm{v,a}}$ and in the distant environment $\rho_{\mathrm{v,env}}$, the density of liquid water ρ_{w} (param. in Hare and Sorensen, 1987; Pruppacher and Klett, 2010, p. 87) and ice ρ_{i} (param. in Baron and Willeke, 2001), the heat capacity of liquid water a c_{w} (param. in Biddle et al., 2013) and ice c_{i} (param. in Pruppacher and Klett, 2010, p. 87) are considered.

In addition to the individual droplet freezing time, the inter-arrival time is also relevant for the understanding of micro- and macroscopical rimer structure in the different growth regimes. Based on the number collision rate, it is possible to estimate the statistical inter-arrival time (t_{i}) between two droplets colliding at the same site on the rimer surface via Eq. 13. Both droplets are considered to form spherical caps upon accretion with base area A_{cap}.

$$t_{\mathrm{i}} = \frac{1}{R_{\mathrm{accr,N}} A_{\mathrm{cap}}} \tag{13}$$

The inter-arrival time is an important parameter for developing rimer surface structure during riming, as described in Sect 3.1.

S5 Rime-splintering experiments at IDEFIX

A detailed overview of all valid rime-splintering experiments comprising the parameter space and observations of riming, SIP and other features is given in Table S3. The few cases, where potential SI particles were detected in the IC during or after riming, are illustrated in Fig. S7 with a pair of a HSV and IC images showing the matured rimer structure and detected ice crystals.

Table S3. Overview of valid rime-splintering experiments in dependence on the main parameters: set air temperature, air velocity, droplet size distribution (DSD). The accreted mass is mainly determined by using HSV method (described in Supplement Sect. S2.1) or * calculated from average mass collision rate and riming time. The validation criteria comprised general functionality tests of the ice counter as well as ice counter background tests before and after each riming experiment and a minimum of approximately 0.1 mg of total accreted rime mass during the experiment. ** in this case, DSD2 was initially unstable and periods of more collisions and larger droplets occurred briefly, leading to local wetting of the ice surface.

T [°C]	$u_{\max}$**[m s^{-1}]**	**experiment**	**DSD**	**growth regime**	**total accreted mass [mg]**	**ice detected, number of crystals**	**ice particle occurrence, special observations**
-4	1	C2_T34	DSD1	dry	0.1–0.2	**no**	
		C2_T38	DSD1	dry	0.1*	**no**	
		C2_T35	DSD2	dry	0.1–0.2	**no**	
		C2_T38b	DSD3	wet	0.1–0.2*	**no**	
-5	1	C1_T09	DSD1	dry	0.2–0.3*	**yes, >20**	during riming
		C1_T12	DSD1	dry	0.1–0.2	**no**	
		C1_T13	DSD1	dry	0.2–0.3	**no**	
		C1_T20	DSD1	dry	0.1–0.2	**no**	
		C2_T59	DSD1	dry	0.1–0.2	**no**	
		C2_T57	DSD2	dry	0.1–0.2	**no**	
		C2_T56	DSD3	wet	0.2	**no**	
	3	C2_T04	DSD1	dry	0.4–0.6	**no**	
		C2_T04b	DSD3	dry	0.1–0.8*	**no**	
		C2_T06	DSD3	dry/transition	0.5–1.4*	**yes, 5**	during riming
	6	C2_T60	DSD1	dry	0.1	**no**	
-7	1	C1_T22	DSD1	dry	0.2–0.4	**no**	
		C2_T15	DSD1	dry	0.1	**no**	
		C2_T19	DSD1 & DSD2 varied	dry	0.1–0.2	**no**	
		C2_T20	DSD1 & DSD2 varied	dry	0.2–0.5	**no**	
	2	C1_T22b	DSD1	dry	0.1–0.2	**yes, 1**	after riming (rime spire break-off)
	3	C2_T12	DSD1	dry	0.1–0.2*	**no**	
-10	1	C2_T39	DSD1	dry	0.1*	**yes, 2**	after riming
		C2_T43	DSD1	dry	0.1–0.3	**no**	
		C2_T40	DSD2	dry	0.1*	**no**	
		C2_T45	DSD2	dry, initially unstable**	0.1*	**no**	ice spicule growth during riming (Fig. 11c)
		C2_T44	DSD4	transition	0.1–0.2	**yes, 1**	after riming, ice spicule growth during riming (Fig. 11e)
		C2_T48	DSD4	transition	1.3	**no**	ice spicule growth during riming (Fig. 11a,b)
		C2_T50	DSD4	transition, dry	0.4–0.5	**no**	ascending air bubbles (Fig. 11d)
	3	C2_T54	DSD1	dry	0.1–0.2	**yes, 1**	after riming (rime spire break-off)
		C2_T53	DSD3	dry	0.5–0.7*	**no**	

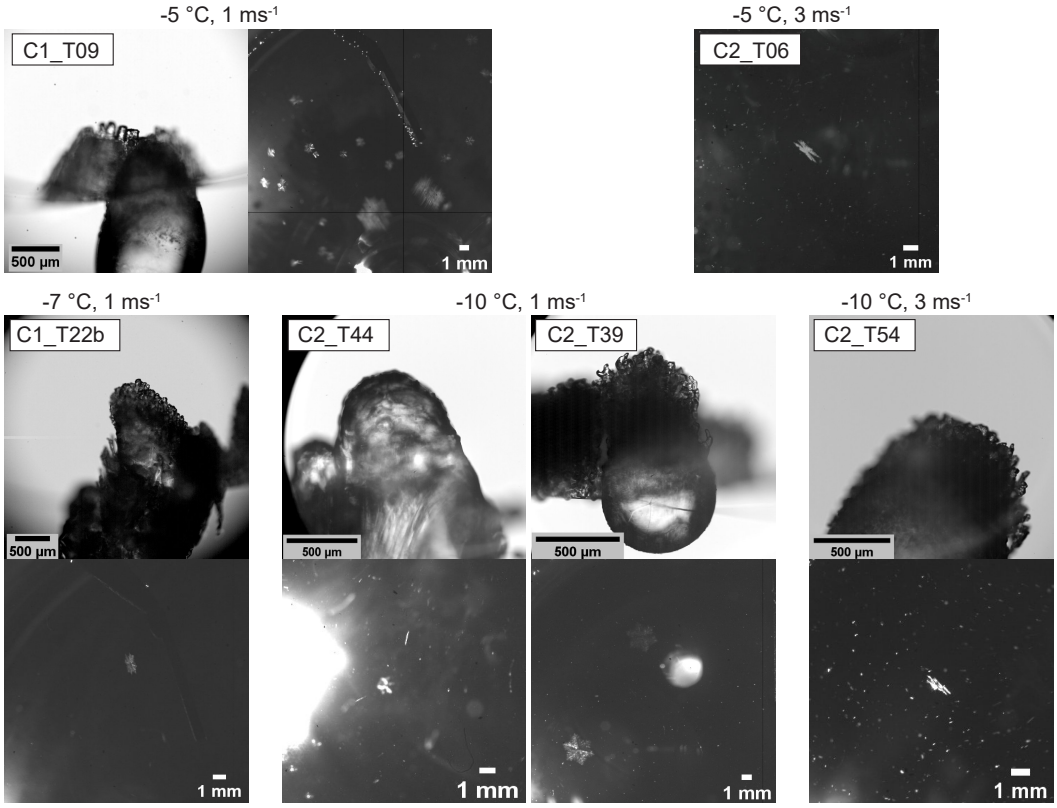

Figure S7. HSV images illustrating the rimed structure of ice targets from experiments in which SIP particles have been detected with the IC together with the corresponding enlarged cut-out of an IC image showing detected ice crystals close to the end of the experiment. A HSV image of C2_T06 is missing due to lack of HSV data.

References

Baron, P. A. and Willeke, K.: Aerosol fundamentals, Aerosol measurement: principles, techniques, and applications, 2, 2001.

Beard, K. and Pruppacher, H. R.: A wind tunnel investigation of the rate of evaporation of small water drops falling at terminal velocity in air, J. Atmos. Sci., 28, 1455–1464, 1971.

Biddle, J. W., Holten, V., Sengers, J. V., and Anisimov, M. A.: Thermal conductivity of supercooled water, Phys. Rev. E, 87, 042 302, 2013.

Cober, S. G. and List, R.: Measurements of the heat and mass transfer parameters characterizing conical graupel growth, J. Atmos. Sci., 50, 1591–1609, 1993.

Erfani, E. and Mitchell, D. L.: Growth of ice particle mass and projected area during riming, Atmos. Chem. Phys., 17, 1241–1257, 2017.

Hall, W. and Pruppacher, H.: The survival of ice particles falling from cirrus clouds in subsaturated air, J. Atmos. Sci., 33, 1995–2006, 1976.

Hare, D. and Sorensen, C.: The density of supercooled water. II. Bulk samples cooled to the homogeneous nucleation limit, J. Chem. Phys., 87, 4840–4845, https://doi.org/https://doi.org/10.1063/1.453710, 1987.

Heymsfield, A. J. and Pflaum, J. C.: A quantitative assessment of the accuracy of techniques for calculating graupel growth, J. Atmos. Sci., 42, 2264–2274, 1985.

Hinds, W. C.: Aerosol technology : properties, behavior, and measurement of airborne particles, New York (N.Y.) : Wiley, 2nd ed. edn., http://lib.ugent.be/catalog/rug01:000658373, 1999.

Jensen, A. A. and Harrington, J. Y.: Modeling Ice Crystal Aspect Ratio Evolution during Riming: A Single-Particle Growth Model, J. Atmos. Sci., 72, 2569–2590, https://doi.org/https://doi.org/10.1175/JAS-D-14-0297.1, 2015.

Korolev, A. and Leisner, T.: Review of experimental studies of secondary ice production, Atmos. Chem. Phys., 20, 11 767–11 797, https://doi.org/10.5194/acp-20-11767-2020, 2020.

Kulkarni, P.: Aerosol measurement: principles, techniques, and applications, Wiley, Hoboken, NJ, 3. ed. edn., http://onlinelibrary.wiley.com/book/10.1002/9781118001684, includes bibliographical references and index. - Print version record, 2011.

Macklin, W.: The density and structure of ice formed by accretion, Quart. J. Roy. Meteorol. Soc., 88, 30–50, 1962.

Macklin, W. and Payne, G.: Some aspects of the accretion process, Quart. J. Roy. Meteorol. Soc., 94, 167–175, 1968.

Murphy, D. M. and Koop, T.: Review of the vapour pressures of ice and supercooled water for atmospheric applications, Quart. J. Roy. Meteorol. Soc., 131, 1539–1565, https://doi.org/https://doi.org/10.1256/qj.04.94, 2005.

Pruppacher, H. and Klett, J.: Microphysics of Clouds and Precipitation, vol. 18, Springer Dordrecht Heidelberg London New York, https://doi.org/10.1007/978-0-306-48100-0, 2010.